



**UNIVERSITY OF LEEDS**

This is a repository copy of *Melting phase relations in the Fe-S and Fe-S-O systems at core conditions in small terrestrial bodies*.

White Rose Research Online URL for this paper:  
<http://eprints.whiterose.ac.uk/128018/>

Version: Accepted Version

---

**Article:**

Pommier, A, Laurenz, V, Davies, CJ [orcid.org/0000-0002-1074-3815](https://orcid.org/0000-0002-1074-3815) et al. (1 more author) (2018) Melting phase relations in the Fe-S and Fe-S-O systems at core conditions in small terrestrial bodies. *Icarus*. ISSN 0019-1035

<https://doi.org/10.1016/j.icarus.2018.01.021>

---

(c) 2018, Elsevier Ltd. This manuscript version is made available under the CC BY-NC-ND 4.0 license <https://creativecommons.org/licenses/by-nc-nd/4.0/>

**Reuse**

This article is distributed under the terms of the Creative Commons Attribution-NonCommercial-NoDerivs (CC BY-NC-ND) licence. This licence only allows you to download this work and share it with others as long as you credit the authors, but you can't change the article in any way or use it commercially. More information and the full terms of the licence here: <https://creativecommons.org/licenses/>

**Takedown**

If you consider content in White Rose Research Online to be in breach of UK law, please notify us by emailing [eprints@whiterose.ac.uk](mailto:eprints@whiterose.ac.uk) including the URL of the record and the reason for the withdrawal request.



[eprints@whiterose.ac.uk](mailto:eprints@whiterose.ac.uk)  
<https://eprints.whiterose.ac.uk/>

1  
2  
3  
4  
5  
6  
7  
8  
9  
10  
11  
12  
13  
14  
15  
16  
17  
18  
19  
20  
21

# **Melting Phase Relations in the Fe-S and Fe-S-O Systems at Core Conditions in Small Terrestrial Bodies**

Anne Pommier<sup>1\*</sup>, Vera Laurenz<sup>2</sup>, Christopher J. Davies<sup>3</sup>, Daniel J. Frost<sup>2</sup>

<sup>1</sup> UC San Diego, Scripps Institution of Oceanography, Institute of Geophysics and Planetary Physics, La Jolla, CA, USA.

<sup>2</sup> Bayerisches Geoinstitut, Universität Bayreuth, Germany.

<sup>3</sup> School of Earth & Environment, University of Leeds, Leeds LS2 9JT, UK.

\*Corresponding author. Pommier@ucsd.edu

## 22 **Abstract**

23 We report an experimental investigation of phase equilibria in the Fe-S and Fe-S-O  
24 systems. Experiments were performed at high temperatures (1400-1850°C) and high  
25 pressure (14 and 20 GPa) using a multi-anvil apparatus. The results of this study are  
26 used to understand the effect of sulfur and oxygen on core dynamics in small terrestrial  
27 bodies. We observe that oxygen has little effect on the liquidus temperature and that  
28 the formation of solid FeO grains occurs at the Fe-S liquid – Fe solid interface at high  
29 temperature (>1400°C at 20 GPa). Oxygen fugacities calculated for each O-bearing  
30 sample showed that redox conditions vary from  $\Delta IW = -0.65$  to 0. Considering the  
31 relative density of each phase and existing evolutionary models of terrestrial cores, we  
32 apply our experimental results to the cores of Mars and Ganymede. We suggest that the  
33 presence of FeO in small terrestrial planets tends to contribute to outer-core  
34 compositional stratification. Depending on the redox and thermal history of the planet,  
35 FeO may also help forming a transitional redox zone at the core-mantle boundary.

36

37

## 38 **1. Introduction**

39 Different light elements (e.g., sulfur, oxygen, hydrogen, nitrogen, carbon, silicon)  
40 could have been added to the Fe-Ni metallic core of terrestrial planets during  
41 differentiation processes (e.g., Poirier, 1994; Wood et al., 2006). It has been suggested  
42 that several wt.% of light elements may compose the core of these planets, such as the  
43 Earth, Mars, and Mercury (e.g., Birch, 1964; Dreibus and Wänke, 1985; Harder and  
44 Schubert, 2001). Sulfur is thought to be a major light element in terrestrial cores due to

45 its high solubility in liquid iron (Dreibus and Wänke, 1985; Dreibus and Palme, 1996;  
46 Allègre et al., 2001) and to the possible segregation of liquid FeS sulfide into the core  
47 (e.g., O'Neill, 1991; Laurenz et al., 2016; Rubie et al., 2016). Earth's core density deficit  
48 of up to about 10 wt.% compared to the density of a pure Fe-Ni core (e.g., Anderson and  
49 Isaak, 2002) is usually assumed to be the result of a combination of several light  
50 elements, as S (or Si) alone cannot satisfy the density jump at the inner core boundary  
51 (i.e. outer core density deficit) while preserving the (astronomically-determined) mass  
52 of the core (e.g., Alfé et al., 2002). One major candidate is oxygen (e.g., Ohtani and  
53 Ringwood, 1984; Ringwood and Hibberson, 1991; Badro et al., 2015) because of its  
54 abundance in the bulk Earth, its partitioning behavior into metal at core pressure and  
55 temperature (Alfé et al., 2002), and because thermodynamic calculations and high-  
56 pressure experiments showed a high solubility of S and O in liquid iron (e.g., Urakawa et  
57 al., 1987; Tsuno and Ohtani, 2009; Buono and Walker, 2015). Considering a Fe-S-O  
58 system, the oxygen abundance in the Earth's present-day core can be as high as ~6  
59 wt.% (McDonough and Sun, 1995; Tsuno et al., 2007; Davies et al., 2015). Because high  
60 solubility of S and O in liquid Fe is observed at shallower pressure than Earth's core  
61 pressure (e.g., Tsuno et al., 2007), it is possible that the metallic core of terrestrial  
62 bodies smaller than the Earth also contains these two light elements in significant  
63 amounts.

64         At the conditions of Earth's inner core boundary, *ab initio* calculations based on  
65 density functional theory suggest that oxygen partitions almost entirely into the liquid  
66 phase on freezing (Alfé et al., 2002). This partitioning depresses the core melting  
67 temperature by 500-1000 K (Davies et al, 2015), which is a key factor in determining

68 the timing of inner core formation. Oxygen rejected from the solid phase as the inner  
69 core freezes is lighter than the overlying liquid and must rise, mixing the outer core  
70 (Braginsky, 1963). The associated gravitational energy release is the most efficient  
71 power source for generating magnetic field and is the dominant contribution to  
72 maintaining the present geodynamo (Lister and Buffett, 1995; Nimmo, 2015). It has  
73 also been proposed that oxygen accumulates below Earth's core-mantle boundary  
74 (CMB), either via chemical reactions with the mantle or by pressure-driven diffusion,  
75 creating a stable stratification (Buffett and Seagle, 2010; Gubbins and Davies, 2013;  
76 [Brodholt and Badro, 2017](#)). However, it is presently unclear whether oxygen plays the  
77 same crucial dynamical role in the core of smaller terrestrial bodies (i.e., at smaller  
78 pressure than Earth's core pressure) as it does in Earth. This gap in our current  
79 understanding of planetary cores at conditions relevant to small terrestrial planets  
80 requires the investigation of the crystallization of O-bearing phases and the partitioning  
81 behavior of oxygen between these phases. It has been suggested that the core of small  
82 terrestrial planets contains only a very small concentration of oxygen, because the  
83 temperatures experienced by these small bodies may not be high enough to partition a  
84 significant amount of oxygen into the metallic core (e.g., Rubie et al., 2004). However,  
85 there is no consensus on the amount of oxygen in the core of these terrestrial planets  
86 yet, and other laboratory-based thermodynamic models proposed that a few wt. % O  
87 may be stored in their core (e.g., Tsuno et al. 2011). In the present study, we consider  
88 the latter hypothesis and examine the effect of oxygen on the crystallization of a Fe-S  
89 core in small terrestrial bodies.

90 Several experimental studies have investigated the effect of oxygen on phase  
91 equilibria of the Fe-S system, but only a few of them were conducted at pressures  
92 relevant to the cores of small terrestrial planets (i.e. up to a few tens of GPa) and near  
93 the liquidus temperature in order to investigate core crystallization processes  
94 (Urakawa et al., 1987; Tsuno et al., 2007, 2011; Tsuno and Ohtani, 2009; Buono and  
95 Walker, 2015). However, these studies conducted in the Fe-S(-O) systems considered  
96 either high S contents (>10 wt.% S in Buono and Walker, 2015 and Tsuno et al., 2011)  
97 or high O contents (>8.0 wt.% O in Tsuno et al., 2007; >3.7 wt.% O in Tsuno and Ohtani,  
98 2009) and thus cannot be used to understand the effect of a small amount of light  
99 elements on core crystallization. Here, we present phase equilibria experiments in the  
100 Fe-S and Fe-S-O systems at 14 and 20 GPa and at high temperatures ( $>T_{\text{eutectic}}$ ). We  
101 conducted experiments on Fe-S samples containing 1 and 5 wt.% S in order to  
102 characterize the meting relationships of core analogues containing a small amount of S.  
103 Constraining the shape of the liquidus curve in the Fe-S system is key to understand the  
104 crystallization processes of cores and requires further experimental constraint, as  
105 previous studies suggested either a parabolic or a sigmoidal shape (Fei et al., 2000;  
106 Chen et al., 2008, respectively). Experimental oxygen fugacities are calculated for each  
107 sample. Experiments in the Fe-S-O system were conducted at pressure and temperature  
108 conditions similar to the experiments on Fe-S in order to allow direct comparison and  
109 characterize the effect of a small amount of oxygen (up to 3 wt.% O) on Fe-S phase  
110 equilibria. Our results are applied to the cores of Mars and Ganymede in order to  
111 constrain the effect of oxygen on the structure and possible evolution of terrestrial  
112 cores as well as their magnetic activity.

113

114

## 115 **2. Experimental methods**

### 116 *2.1. Starting materials*

117 Experimental samples consist of Fe-S and Fe-S-O mixtures that were synthesized  
118 from FeS and Fe powders in various proportions, with the addition of Fe<sub>2</sub>O<sub>3</sub> for the O-  
119 bearing materials. Each mixture was placed in a drying oven at about 150°C for several  
120 hours and then stored in a desiccator. Five compositions were obtained and atomic  
121 proportions are listed in Table 1. No nickel was added to our starting materials as  
122 previous work pointed out that adding Ni to the Fe-S system does not significantly  
123 affect the liquidus temperature and phase relations of Fe and Fe-S (Stewart et al., 2007;  
124 Martorell et al., 2013) [though this small effect can be observed \(Zhang and Fei, 2008\)](#).

125

### 126 *2.2. Phase equilibrium experiments*

127 Experiments were performed at 14 and 20 GPa and at temperatures ranging  
128 from 1400 to 1850°C. All experiments were performed in a Kawai-type multi-anvil  
129 apparatus using tungsten carbide cubes with a corner-truncation edge length of 4 mm  
130 and MgO (doped with 5 wt.% Cr<sub>2</sub>O<sub>3</sub>) octahedral pressure media with an edge length of  
131 10 mm. The samples were placed in either high purity MgO single crystal capsules or  
132 Al<sub>2</sub>O<sub>3</sub> tubing topped with MgO spacers, and surrounded by a LaCrO<sub>3</sub> heater. The  
133 assembly was dried in a furnace at 1000°C before the experiment. The thermal gradient  
134 inside the sample is estimated to be in the order of 10-20°C/mm (Rubie, 1999, Buono  
135 and Walker 2015). Some experiments contained two sample capsules on top of each

136 other that were run simultaneously. A type D  $W_{97}Re_3$ - $W_{75}Re_{25}$  thermocouple was  
137 placed in contact with the top MgO spacer through the heater, and in case the  
138 thermocouple was lost during an experiment, the power-temperature relationship was  
139 used to estimate temperature. Run duration was 20 min at the highest temperatures  
140 (1760 and 1850°C) and 30 min at lower temperatures (Table 1). Previous work on the  
141 monitoring of thermal and chemical equilibrium in the Fe-S system showed that this is  
142 sufficient time at these pressure and temperature conditions to obtain a homogeneous  
143 chemical composition, indicating that chemical and phase equilibrium was reached  
144 (Chen et al., 2008a). The experiments were ended by quenching, i.e., by turning off the  
145 power to the heater. Recovered samples were mounted in epoxy and polished for  
146 chemical analyses.

147

### 148 *2.3. Analytical techniques*

149 Recovered samples were polished for microscope and electron microprobe  
150 analyses at the Bayerisches Geoinstitut. Textural analyses of the quenched samples  
151 were used to determine melting relations. Chemical analyses of the recovered samples  
152 and MgO capsules were performed using an electron microprobe (Jeol JXA-8200) with  
153 15 kV accelerating voltage and 15 nA beam current. Counting times were 20 s for major  
154 elements and 10 s for background. Standards were metallic iron or  $Fe_2O_3$  for Fe  
155 (depending on the phase analyzed),  $FeS_2$  for S, MgO or  $Fe_2O_3$  for O, and enstatite for Mg.  
156 The ZAF correction method was used for matrix corrections. All solid phases were  
157 analyzed using a focused beam. Because sulfide and metallic melts show quench  
158 textures, they were analyzed using a defocused beam of 20  $\mu m$  in diameter. Bulk



159 chemical compositions were obtained by averaging grid analyses (3x3 points along  
160 grids of 60 $\mu$ m $\times$ 60 $\mu$ m). Several of these grids were analyzed and each grid-average was  
161 taken as a single analysis from which final averages and standard deviations were  
162 calculated (Table 2). This procedure has previously been shown to yield comparable  
163 results to estimating bulk compositions via image analysis (Chabot and Drake, 1997).

164

165

166

### 167 **3. Results**

#### 168 *3.1. Sample textures and phase relations*

169 The experimental conditions and observed phase assemblages are summarized  
170 in Table 1 and the chemical composition of each phase is listed in Table 2.

171

##### 172 3.1.1. Fe-S binary system

173 Back-scattered electron (BSE) images of several experiments are presented in  
174 Figure 1. Samples with Fe-S starting composition either show a single quenched liquid  
175 phase or both metallic iron and a liquid phase that quenched to iron dendrites in the Fe-  
176 S matrix (Figure 1). Small amounts of oxygen in these experiments were measured in  
177 the liquid phase and a few small FeO grains were observed in some retrieved samples  
178 (Figure 1c, Table 2). The presence of minor amounts of O in these samples possibly  
179 results from interactions with surrounding materials (capsule and/or heater).

180 Using the textures obtained from experiments at different temperatures, we  
181 inferred a portion of the liquidus curve in the Fe-FeS system at 14 GPa and 20 GPa

182 (Figure 2). At 14 GPa, our results are consistent with the ones by Chen et al. (2008a) at a  
183 similar pressure but are different from the predicted liquidus by the thermodynamic  
184 model by Buono and Walker (2011). As underlined by Buono and Walker (2011), this  
185 can be explained by a change in the thermodynamic behavior of the liquid that occurs  
186 above 10 GPa. At 20 GPa, the determination of the liquidus curve from our data at about  
187 5wt.% S does not agree with the predicted liquidus curve from Fei et al. (2000) at 21  
188 GPa: for this composition, Fei et al. predicted a liquidus temperature of 1900°C, while  
189 an additional data point from our experiments suggests a temperature of  $\approx 1700^\circ\text{C}$  (+/-  
190 50) that would be consistent with a sigmoidal shape of the liquidus curve, though our  
191 data cannot confirm that the shape at 20 GPa is sigmoidal. We observe a steep slope of  
192 the liquidus curve between 2000 and about 1600°C and a relatively flat slope near  
193 1500°C. Our data would be consistent with an inflection point at about 7wt.% S. This  
194 has previously been observed in the Fe-S system over a wide pressure range for a  
195 similar sulfur content (at 14 GPa, Chen et al., 2008a; from 15 to 20.6 GPa, Andrault et al.,  
196 2009; from 1 bar to 10 GPa, Buono and Walker, 2011 and references therein) and  
197 indicates a non-ideal liquid solution behavior with a metastable solvus beneath the  
198 liquidus. Such a sigmoidal shape is characteristic of a metastable miscibility gap (i.e.  
199 metastable with respect to solid Fe and liquid) at temperatures below the inflection  
200 point of the liquidus (e.g., Buono and Walker, 2011).

201 Three experiments were conducted with starting materials containing 36.5 wt.%  
202 S. Solid FeS was observed in the three experimental products, as is expected from phase  
203 equilibria, but the absence of a liquid phase in two of them (S6421 and S6535b) is not in  
204 agreement with previous phase diagrams (Fei et al., 2000; Chen et al., 2008a). This

205 might be explained by the fact that these experiments are close to the boundary  
206 between FeS + liquid field and the field of single solid solution pyrrhotite  $\text{Fe}_{1-x}\text{S}$   
207 expected at 35 wt.%S (Ehlers, 1972). A small oxidation of Fe into FeO in these  
208 experiments leaves the bulk composition with a higher S content (i.e., >36wt.%), and  
209 thus, the solids obtained in our experiments are solid phases stable at sulfur contents  
210 >35wt.% S.

211

### 212 3.1.2. Fe-S-O ternary system

213 As illustrated in Figure 3a, samples of Fe-S-O starting composition quenched  
214 from above the liquidus temperature present quenched liquid made of Fe-dendrites, Fe-  
215 S matrix, and rosaceous FeO grains (compositions listed in Table 2). For samples  
216 quenched from below the liquidus temperature, BSE-images show that the phases are  
217 metal Fe and solid FeO coexisting with a liquid phase composed of Fe-dendrites and a  
218 Fe-S matrix (Figure 3b-f). Several FeO-rich blobs were observed in large metallic iron  
219 grains and may represent exsolution products from the Fe-metal phase (Figure 3b). It  
220 should be noted that in all Fe-S-O experiments, the use of MgO capsule leads to the  
221 formation of a thin ferropericlase layer at the sample-capsule interface, due to the  
222 reaction between iron and MgO (Figure 3).

223 Extensive crystallization of solid FeO at the interface between solid iron and  
224 liquid phase (Figure 3c-f) was observed in all oxygen-added experiments except in two  
225 runs performed at 20 GPa (Table 1): S6426, which was conducted above the liquidus  
226 temperature (Figure 3a) and S6428, which was the experiment performed at the lowest  
227 temperature (1400°C, Figure 3b). At lower pressure (14 GPa), a continuous FeO layer

228 was observed at 1400°C. In runs performed at temperatures close to the liquidus  
229 (which depends on both composition and pressure: 1600°C at 20 GPa, and 1400-  
230 1500°C at 14 GPa), the FeO layer is partially broken up (Figure 3d-f), with one side of  
231 the layer showing FeO grains dissociated from the layer and being disseminated into  
232 the melt phase. The following observations can be made regarding the stability of the  
233 FeO layer: 1) at 20 GPa, the FeO layer is only observed at temperature higher than  
234 1400°C, whereas it is present at 14 GPa and 1400°C and 2) at high temperature, the  
235 layer is broken and FeO grains move towards the liquid phase. Further work is required  
236 to determine whether or not the texture of the layer depends on its thickness, and if a  
237 threshold in the layer thickness exists, above which the layers breaks down into FeO  
238 grains. No effect of the bulk oxygen content (up to 3 wt.% O) is observed on the stability  
239 of the layer, since experiments containing 0.65 and 3 wt.% O performed at the same  $P$ ,  $T$   
240 conditions both present this structure of FeO grains (S6435 and S6433a, Table 1).

241 Electron microprobe traverses performed across the interfaces between O-  
242 bearing samples and the MgO capsule indicate the formation of a nearly continuous  
243 layer of ferropicriase (Figures 3e-f and Section 3.2). However, these reaction rims are  
244 only about 10 micron thick, and microprobe analyses across the sample and away from  
245 this layer showed homogeneous chemistry of each phase throughout the capsule.

246

### 247 *3.2. Solubility of oxygen and sulfur in the metal and melt phase*

248 In both Fe-S and Fe-S-O experiments, oxygen content in solid iron is negligible  
249 (Table 2), which is in agreement with oxygen contents reported by Tsuno and Ohtani  
250 (2009) and Tsuno et al. (2011). The amount of sulfur dissolved in solid iron increases

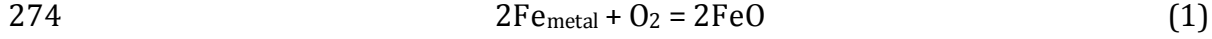
251 with decreasing temperature from 0.2 to 0.5 at.% S (Figure 4a) and the absence of  
252 solubility of S in FeO was observed. These sulfur contents are in agreement with  
253 previous studies at comparable pressure (Li et al., 2001; Stewart et al., 2007; Tsuno and  
254 Ohtani, 2009). When temperature is below the liquidus, solid iron is in equilibrium with  
255 the Fe-S liquid that has less and less sulfur when temperature increases, due to the  
256 dilution effect. With increasing temperature, the activity of sulfur in the Fe-S melt  
257 decreases, which leads to a decrease in the sulfur content in the coexisting solid iron.

258 For Fe-S-O experiments crystallizing FeO, the samples are FeO buffered,  
259 suggesting that we can constrain the O content of both Fe metal and coexisting liquid in  
260 terms of the effects of T and S-content. Sulfur and oxygen solubilities in the liquid phase  
261 are presented in Figures 4b and 4c. At low temperature (1400°C), the first liquids  
262 produced are sulfur-rich, containing up to 28 at.% S (Figure 4b), which promotes the  
263 incorporation of oxygen into the liquid phase. As shown in Figure 4c, the oxygen  
264 content in the liquid increases with temperature (from 0.7 to 3.2 at.% on the  
265 investigated  $T$  range). Increasing temperature increases the ability of the liquid to  
266 dissolve oxygen and decreases the sulfur content of the liquid by dilution effect. At  
267 higher temperature (>1800°C), a decrease of the oxygen content in both liquid and solid  
268 is expected, due to the effect of decreasing the sulfur content.

269

### 270 *3.3. Oxygen fugacity determination*

271 For experiments in the Fe-S (-O) system, Fe-metal is generally in equilibrium  
272 with an FeO-bearing oxide (either pure FeO or ferropericlase), so that the oxygen  
273 fugacity of the sample can be defined by the following redox reaction



275 for which the equilibrium constant can be written as follows

276 
$$K(1) = \log \left[ \frac{(a_{\text{FeO}})^2}{(a_{\text{Fe}}^{\text{metal}})^2 f_{\text{O}_2}} \right] = 2 \log \left[ \frac{X_{\text{FeO}}}{X_{\text{Fe}}^{\text{metal}}} \right] + 2 \log \left[ \frac{\gamma_{\text{FeO}}}{\gamma_{\text{Fe}}^{\text{metal}}} \right] - \log f_{\text{O}_2}^{\text{exp}}$$
 (2)

277 where  $f_{\text{O}_2}^{\text{exp}}$  denotes the oxygen fugacity of the experiment and  $a_i$ ,  $X_i$  and  $\gamma_i$  are the  
 278 activities, mole fractions and activity coefficients of  $i$  (i.e., Fe and FeO), respectively. If  
 279 pure Fe is in equilibrium with pure FeO (i.e.  $a_{\text{Fe}} = a_{\text{FeO}} = 1$ ), equilibrium (1) defines the  
 280 Iron-Wüstite buffer and  $K(1) = -\log f_{\text{O}_2}^{\text{IW}}$ . Substituting this relationship into Eq. (2)  
 281 yields

282 
$$\log f_{\text{O}_2}^{\text{exp}} - \log f_{\text{O}_2}^{\text{IW}} = 2 \log \left[ \frac{X_{\text{FeO}}}{X_{\text{Fe}}^{\text{metal}}} \right] + 2 \log \left[ \frac{\gamma_{\text{FeO}}}{\gamma_{\text{Fe}}^{\text{metal}}} \right] = \Delta \text{IW}$$
 (3)

283 The oxygen fugacity of the experiments can therefore be expressed relative to the IW-  
 284 buffer using Eq. (3). In many experiments, pure Fe metal is in equilibrium with pure  
 285 FeO, so that  $\Delta \text{IW} = 0$ . If no pure FeO phase is present to calculate  $f_{\text{O}_2}$ , we used  
 286 ferropericlase that formed as a result of the reaction of the sample with the MgO single  
 287 crystal capsule. Taking into account the activity composition relations in ferropericlase  
 288 (Frost et al., 2003) and assuming that Raoult's Law is valid (i.e.,  $\gamma_{\text{Fe}}^{\text{metal}} = 1$ ) (Mann et al.,  
 289 2009), the experimental  $f_{\text{O}_2}$  can be expressed relative to the Iron-Wüstite buffer using  
 290 the following equation (Mann et al., 2009)

291 
$$\Delta \text{IW} = 2 \log \left[ \frac{X_{\text{FeO}}^{\text{ferrop.}}}{X_{\text{Fe}}^{\text{metal}}} \right] + \frac{2(11,000 + 0.011P)(1 - X_{\text{FeO}}^{\text{ferrop.}})^2}{RT \ln 10}$$
 (4)

292 with  $P$  the pressure (bar),  $T$  the temperature (K), and  $R$  the universal gas constant. For  
 293 all samples from the Fe-S system containing small amounts of oxygen, at both 14 and 20  
 294 GPa,  $\Delta \text{IW}$  ranges from -0.65 to -0.13 (Figure 5 and Table 2), whereas experiments in the

295 Fe-S-O system being FeO buffered,  $\Delta IW=0$ . There is no noticeable effect of temperature  
296 on the calculated  $fO_2$ , suggesting that the absolute  $fO_2$  of the experiments evolves  
297 parallel to the buffer with changing  $T$ .

298

299

## 300 **4. Discussion**

### 301 *4.1 Formation and stability of FeO grains at the melt-solid iron interface in* 302 *laboratory experiments and in planetary cores*

303 We suggest that the formation of FeO results from a compositional gradient in  
304 oxygen in the sample initiated by a small thermal gradient across the capsule. When Fe-  
305 S-O melt contains metal iron, the melt separates from the residual solid phase due to a  
306 small temperature gradient, rather than density contrast (Walker, 2000). The presence  
307 of a small thermal gradient would favor the accumulation of solid metal in the cold end  
308 of the capsule (Buono and Walker, 2015). The process is independent from the relative  
309 density of each phase, as it has been shown that dense solid iron can accumulate at the  
310 top of the capsule (Walker, 2000). This observation contrasts significantly with a  
311 planetary core, in which the buoyancy force points in the direction of gravity. In terms  
312 of oxygen solubility in the liquid, the thermal gradient associated with the accumulation  
313 of solid metal in the cold part of the capsule results in a gradient in oxygen solubility  
314 within the liquid phase: oxygen solubility in the liquid decreasing with temperature  
315 (Figure 4c), it is the smallest at the solid-melt interface, i.e. where temperature is the  
316 lowest. Because oxygen solubility is negligible in solid iron, the solid-melt interface

317 starts forming FeO grains. We suggest that the stability of the FeO grains is due to  
318 changes in oxygen solubility in the melt, probably as a function of temperature.

319         The presence of an FeO layer has also been reported by Buono and Walker  
320 (2015) at 6-8 GPa and was thought to be immiscible FeO liquid, whereas Tsuno et al.  
321 (2011) suggested that FeO is present as a solid phase in their experiments at 5-24.5  
322 GPa. It is reasonable to assume that FeO in our experiments and in these previous  
323 studies is solid for three major reasons: 1) The melting temperature of FeO is  $\approx 1470^\circ\text{C}$   
324 at 8 GPa,  $\approx 1650^\circ\text{C}$  at 14 GPa and  $\approx 1950^\circ\text{C}$  at 20 GPa (Fischer and Campbell, 2010),  
325 which is a much higher temperature than the one in the experiments of Buono and  
326 Walker ( $< 1100^\circ\text{C}$ ) and in our experiments; 2) The Fe-oxides in the experiments are  
327 slightly non-stoichiometric, which could affect the melting temperature of the system.  
328 However, Komabayashi (2014) pointed out that at about 14 GPa on the O-rich side of  
329 the immiscibility gap, the lowest melting temperature for an ionic melt at the  
330 monotectic point with about 20 wt.% O (corresponding to a composition comparable to  
331 the one of our Fe oxides) is  $\approx 1880^\circ\text{C}$ , which is still higher than the temperature of  
332 Buono and Walker's experiments as well as our experiments; 3) Textural observations  
333 of the quenched samples suggest that the texture of the FeO layer is very different from  
334 the one of the quenched ionic liquid shown in Tsuno et al. 2011, and the angular  
335 appearance of the FeO grains in the solid Fe metal also suggests that FeO is solid.

336         The solid/liquid interface being an energetically favorable interface to the  
337 formation of FeO grains, FeO crystals can also form at the solid/liquid interface of a  
338 partially crystallized Fe-S-O planetary core. Another point in common to a cooling core  
339 and the experiments regards the solubility of oxygen in the melt phase, which decreases



340 with temperature (Figure 4c). This eventually results in the crystallization of FeO  
341 grains, preferentially at the solid-liquid interface. The formation of FeO grains is  
342 expected in the core, as phase equilibria apply both at the capsule scale and the core  
343 scale. However, we propose that the stability of FeO grains in a planetary core is due to  
344 a mechanism that is different from the one observed in the experiments because of the  
345 importance of buoyancy, whereas the driving forces that control the stability of FeO in a  
346 capsule are constrained by a small volume of core material and a small thermal  
347 gradient.

348

## 349 *4.2. Application to planetary cores*

### 350 *4.2.1. The fate of oxygen in a cooling core*

351 The dynamo in a fully or partially liquid core generates an intrinsic magnetic  
352 field. Depending on the cooling history of the planet, a dynamo may be powered by  
353 compositional convection (e.g., Hauck et al., 2006; Rückriemen et al., 2015), thermal  
354 convection (e.g., Stevenson et al., 1983; Williams and Nimmo, 2004; Kimura et al., 2009;  
355 Dumberry and Rivoldini, 2015), impact-induced changes in the rotation rate (Le Bars et  
356 al., 2011), or mechanical stirring (Dwyer et al., 2011). In all cases, the chemistry and  
357 structure of the core plays a critical role (e.g., Breuer et al., 2015). Here we consider a  
358 convection-driven dynamo and we use experimental results to assess its evolution  
359 during core cooling.

360 We consider sulfur concentrations in planetary cores to be below the eutectic  
361 Fe-S value (from 5 to 15 wt.% S), in agreement with the sulfur content estimated in the  
362 core of Mars (e.g., Dreibus and Wänke, 1985, Sanloup et al., 1999) and Ganymede (e.g.,

363 Hauck et al., 2006), though a FeS core with 36.5 wt.% S has also been suggested for the  
364 latter (Kimura et al., 2009). The eutectic composition varies with pressure, and  
365 corresponds to about 15wt.% S at 20 GPa and 18wt.% S at 14 GPa, *i.e. at Mars CMB*  
366 *conditions* (Figure 2; Fei et al., 2000; Chudinovskikh and Boehler, 2007; Chen et al.,  
367 2008a; Buono and Walker, 2015). *The eutectic composition is not expected to have less*  
368 *than about 13.5 wt% over the entire depth of the Martian core (Mori et al., 2017).*  
369 Considering compositions below the eutectic implies that crystallization in the Fe-FeS  
370 system produces solid phases (metal iron at high temperature and Fe<sub>3</sub>S at low  
371 temperature, Figure 2) that are denser than the Fe-S liquid. If oxygen is present in  
372 planetary cores (e.g., Rubie et al., 2004, Tsuno et al., 2011), its presence during core  
373 crystallization results in the formation of solid FeO coexisting with solid Fe and with  
374 little oxygen present in the coexisting liquid phase (Table 2), as observed in our  
375 experiments containing 0.65 and 3 wt.% O and in previous works (Urakawa et al., 1987;  
376 Tsuno and Ohtani, 2009; Buono and Walker, 2015). As explained above, FeO grains are  
377 expected to crystallize at the interface between solid Fe and Fe-S liquid. The fate of this  
378 region depends on the thermal structure and crystallization regime of the core as well  
379 as the relative density of each phase.

380 Three possible crystallization regimes have been identified in terrestrial cores  
381 for sulfur concentrations below the eutectic, depending on the depth of the intersection  
382 of the adiabat with the melting curve (e.g., Breuer et al., 2015): 1) if  $\partial T_{liquidus}/\partial P >$   
383  $\partial T_{adiabat}/\partial P$  at all  $P$ , a solid inner core grows radially outward, and gravitational energy  
384 is provided by sulfur partitioning into the liquid phase; 2) if  $\partial T_{liquidus}/\partial P < \partial T_{adiabat}/\partial P$  at  
385 all  $P$ , crystallization begins at the outermost part of the core and follows an iron

386 “snowing” regime; 3) in case the relative slopes of  $T_{adiabat}$  and  $T_{liquidus}$  vary with pressure,  
387 crystallization begins in the middle of the core and proceeds towards both the center  
388 and the CMB.

389 In a Fe-S-O core, the evolution of each crystallization regime will depend on the  
390 relative density of O-bearing and S-bearing phases. Previous work observed that  
391 metallic iron is denser than liquid Fe-S and solid FeO at core pressure (e.g., Huang et al.,  
392 2011), implying that upon crystallization at any depth, metallic iron will sink towards  
393 the center of the planet. Comparison between density studies on FeS liquid, FeS solid,  
394 and FeO solid (Sanloup et al., 2000; Balog et al., 2003; Murakami et al., 2004; Kondo et  
395 al., 2004; Urakawa et al., 2004; Nishida et al., 2008, Huang et al., 2011) suggests that 1)  
396 the density of liquid Fe-S is higher than the density of solid FeS if the sulfur content in  
397 the liquid is less than 30wt.%, which is the case for the considered compositions of the  
398 planetary cores; 2) little difference exists between the density of FeS solid and FeO solid  
399 at  $P < \approx 80$  GPa; the Hugoniot curves for FeO and FeS (in the form of FeS-IV) predict only  
400 a slightly lower density for FeO than for FeS (about 0.5 g/cc of difference), and  
401 experimental data by Huang et al. (2011) report an even smaller density difference; 3)  
402 at  $P > 6$  GPa and high temperature, solid FeO is less dense than a Fe-S liquid containing  
403 10 wt.% S. Therefore, we consider that the densities of the first phases to crystallize in a  
404 Fe-S-O core range as follows

$$405 \quad \rho_{\text{Fe metal}} > \rho_{\text{FeS liquid}} > \rho_{\text{FeO solid}} \sim \rho_{\text{FeS solid}}, \quad (5)$$

406 implying that FeO is expected to migrate upward and potentially pile up at the CMB  
407 whereas metallic Fe will tend to sink. This also suggests that if a partially or fully  
408 crystallized core contains oxygen that does not significantly partition into the mantle,

409 then the outermost part of it will tend to be enriched in oxygen through time whereas  
410 the innermost part will tend to be depleted, independently of the crystallization regime  
411 (bottom, top, or middle crystallization).

412 In case the crystallizing S-bearing phase is  $\text{Fe}_3\text{S}$  (and not Fe or FeS), core  
413 dynamics will strongly depend on the resulting density profile of the core, as discussed  
414 in detail in Breuer et al. (2015). For instance, in the case of top-down crystallization,  
415 solid  $\text{Fe}_3\text{S}$  being denser than the residual fluid (Stewart et al., 2007), it is expected to  
416 sink and remelt at depth in a process similar to the iron snow regime (Breuer et al.,  
417 2015). However,  $\text{Fe}_3\text{S}$  crystallization results in increasing density with depth due to an  
418 increase in S content with depth, which is a gravitationally unstable situation, affecting  
419 the long-term dynamics of the core. Comparison of density measurements of FeO and  
420  $\text{Fe}_3\text{S}$  at 300K (Huang et al., 2014 and Kamada et al., 2014, respectively) suggest that  
421  $\text{Fe}_3\text{S}$  is slightly denser than FeO at similar pressure. This suggests that FeO is expected  
422 to migrate upward, though core dynamic modeling studies are required to assess the  
423 effect of  $\text{Fe}_3\text{S}$  crystallization on FeO upward migration.

424

#### 425 *4.2.2. The effect of FeO on the heat budget of a cooling core*

426 Like most crystallization reactions, the formation of FeO is exothermic (e.g., Alfè  
427 et al., 2002). When scaled to a planetary core, this production of heat from FeO  
428 formation may have consequences on the thermal structure and hence the dynamics of  
429 the core. The heat of reaction associated to FeO crystallization can provide an entropy  
430 source for the dynamo, but a detailed investigation is needed to determine its  
431 importance compared to the other entropy sources that depend on the cooling rate.

432           The presence of solid FeO in a metallic core will also influence the gravitational  
433 energy and the latent heat. In our experiments, FeO grains are sandwiched between  
434 solid and liquid Fe-S, a potentially gravitationally unstable configuration. In applying  
435 this result to planetary cores (Figure 6), we first consider the case where freezing  
436 produces solid Fe underlying the FeO layer. Top-down freezing yields continuous  
437 crystallization of Fe and also produces FeO grains trapped beneath the CMB owing to its  
438 density deficit (assuming negligible mass exchange with the mantle), while the solid Fe  
439 falls and remelts, mixing the underlying Fe-S liquid owing to its excess density. The  
440 dynamics are expected to be similar to the standard iron snow regime. If freezing  
441 initiates at greater depths then solid Fe will fall while the buoyant FeO layer will rise,  
442 possibly remelting as discussed below. In this scenario gravitational energy is released  
443 as the FeO grains migrate upwards, which can act to power core convection and  
444 dynamo action. In a case where freezing produces solid iron laying atop FeO, the  
445 configuration is dynamically unstable and mixing between the two solid layers will  
446 inevitably ensue. Whether and how a solid inner core grows in these conditions is not  
447 known at present.

448           The production of FeO on freezing leads to the release of latent heat, which may  
449 be partially balanced by latent heat absorption if dynamic instability results in  
450 remelting of FeO. In bottom-up freezing the latent heat released by freezing out the FeO  
451 crystals at the inner core boundary will add to that produced by freezing out FeS solid;  
452 both act as power sources for core convection and dynamo action (Gubbins et al., 2003).  
453 However, since the FeO grains are lighter than the overlying Fe-S liquid, they will  
454 presumably rise and remelt at shallower depth, absorbing latent heat. Remelting at

455 shallow depth is consistent with the melting curve of FeO at low pressure (e.g.,  
456 Komabayashi, 2014). The net latent heat released or absorbed in this process will  
457 depend on the melting gradient, but recent models of a similar process suggest it will be  
458 small at the core conditions of small terrestrial bodies, such as Ganymede (Rückriemen  
459 et al., 2015). Alternatively, in top-down freezing the latent heat released by FeO  
460 formation will not be balanced by remelting since the layer is buoyant. However, latent  
461 heat release at the top of the core provides very little entropy even though it may  
462 provide a lot of heat, a situation that is likely to stifle dynamo action (Davies and  
463 Pommier, in press).

464         Determining which of these competing effects governs core dynamics will  
465 depend on the structure and history of the planet considered. Another effect that could  
466 influence dynamo activity is liquid immiscibility, which has not been observed in our  
467 experiments but was obtained in previous work conducted at temperature higher than  
468 our maximum  $T$  (e.g. Tsuno et al., 2007). Early in its history, a core may be entirely  
469 molten due to the combined effects of accretionary and radioactive heating. If the  
470 cooling of the Fe-S-O core through time is slow and keeps temperature above the  
471 liquidus and above 2000°C, then liquid FeO coexists with one or two immiscible liquids  
472 (ionic and metallic) at  $P < 20$  GPa and the immiscibility gap disappears at pressure  
473 higher than 21 GPa (Tsuno et al., 2007). If the cooling of a Fe-S-O core through time is  
474 fast, then the core crystallizes rapidly and the lack of a significant liquid phase may  
475 cause the dynamo to stop. The fluid dynamics also depend on the state of FeO (solid or  
476 liquid) as it migrates across the core, and it is unclear how liquid immiscibility in the  
477 Fe-S-O system will affect the heat flux of the cooling core.

478

479 *4.2.3. Implications for Mars and Ganymede: the effect of oxygen on the*

480 *magnetic activity of the core*

481 Past missions have detected different magnetic activities on Mars and  
482 Ganymede: Mars does not currently possess an internally-generated magnetic field but  
483 likely had an ancient magnetic field (Acuña et al., 1999; Solomon et al., 2005), while  
484 Ganymede presents strong magnetic field (Kivelson et al., 1996).

485 Figure 7 compares the present-day thermal structure of Mars and Ganymede  
486 with results of phase equilibria experiments in the Fe-S-O system, and in particular the  
487 conditions for which FeO grains are observed from our experiments and previous  
488 experimental studies. For each planet, the adiabats come from modeling studies  
489 (Breuer et al., 2015 for Ganymede; Williams and Nimmo, 2004, Hauck and Phillips,  
490 2002 for Mars). Considering a Fe-S-O core composition, this figure suggests that the  
491 three cores possibly contain FeO today, and may have formed FeO early in their history  
492 in case they cooled down rapidly, which seems to have been the case for Mars (Williams  
493 and Nimmo, 2004; Breuer and Spohn, 2006).

494 Being the most oxidized terrestrial body with a high FeO content in the mantle  
495 (17.9 wt.% FeO, Dreibus and Wänke, 1985), Mars may have stored a large amount of  
496 oxygen in its core. Though several previous studies have found acceptable thermal  
497 histories for Mars that involve no core crystallization, some hypothesized a plausible  
498 alternative scenario that requires partial crystallization of the core (Stewart et al.,  
499 2007), suggesting that Mars may have entered a snow regime in the past (Davies and  
500 Pommier, in press). As shown in Figure 6 (top panel), the crystallization of metal iron in

501 a snow regime (possibly containing some FeO exsolution) at the CMB and the formation  
502 of solid FeO at the metal iron - liquid Fe-S interface are gravitationally unstable, due to  
503 the high density of the metallic phase. The sinking of dense pure Fe would cause the  
504 disruption of the FeO layer and the upward migration of less dense FeO (Figure 6, top  
505 panel). As a result, if oxygen is present in the Martian core, it has been in the solid form  
506 as FeO for most of its time-evolution and the equilibrium state should be one of stable  
507 chemical stratification beneath the CMB. Regarding the redox state of the planet's core,  
508 it should be close to  $\Delta IW$  due to the presence of FeO (Figure 5). This value is close to  
509 estimates of redox conditions for the mantle, thought to be  $\Delta IW \sim -1$  (e.g., Righter et al.,  
510 2016 and references therein; Figure 5), suggesting that the difference in redox  
511 conditions between the outer core and the lower mantle may be too small for chemical  
512 stratification at the Martian CMB to act as a redox transition zone.

513 The dynamics of Ganymede's core is poorly constrained and its intrinsic  
514 magnetic field (Kivelson et al., 1996) and moment of inertia (Schubert et al., 2004) have  
515 been explained both by compositional (Hauck et al., 2006; Bland et al., 2008) and  
516 thermal dynamos (Kimura et al., 2009). Our results in the Fe-S-O system suggest that  
517 the formation of solid FeO could affect the efficiency of a compositional dynamo, by  
518 forming a FeO-rich layer in the outermost core and reducing the thermal gradient  
519 across the core by releasing heat. An iron snow regime has been proposed for  
520 Ganymede's core (Hauck et al. 2006; Christensen 2015; Rückriemen et al. 2015) and the  
521 present-day estimates for the thermal structure of the core (from 1250 to 1750K in the  
522 pressure range 6-10 GPa, Breuer et al., 2015) are compatible with the presence of solid  
523 FeO (Urakawa et al., 1987). Beside sulfur and possibly oxygen, Ganymede's core, like



524 other terrestrial cores, may contain other volatile elements (such as hydrogen,  
525 Shibazaki et al., 2011) and further work is required to assess the effect of these  
526 elements on dynamo activity.

527

528

529

530

## 531 **5. Conclusions**

532 Phase equilibria experiments in the Fe-S and Fe-S-O systems at 14 and 20 GPa  
533 and at temperature up to 1760°C suggest that oxygen has little effect on the liquidus  
534 temperature. FeO crystallizes in the form of solid grains at the Fe-S liquid – Fe solid  
535 interface. At 20 GPa, this FeO-rich interface is stable from  $T > 1400^\circ\text{C}$  up to 1760°C.  
536 Redox conditions vary from  $\Delta IW = -0.65$  to 0, based on oxygen fugacities calculated for  
537 each sample. Using our experimental results and density constraints, we examine the  
538 effect of oxygen in the core of Mars, Mercury, and Ganymede, and suggest that the  
539 presence of FeO in small terrestrial planets tends to contribute to outer-core  
540 compositional stratification. Depending on the redox and thermal history of the planet,  
541 FeO may also help forming a transitional redox zone at the core mantle boundary.

542

543

544

## 545 **Acknowledgements**

546 We thank all the technical personnel at BGI for their invaluable help with sample  
547 preparation and assistance with microprobe analyses. AP acknowledges funding from  
548 the Alexander von Humboldt Foundation. VL was supported by the European Research  
549 Council Advanced Grant 'ACCRETE' (contract number 290568, awarded to D. Rubie).  
550 Pursuant to AGU guidelines, all the data for this paper are provided within the  
551 publication pages and can further be made available upon request. CD is supported by  
552 Natural Environment Research Council independent research fellowship  
553 NE/L011328/1 and a Green scholarship at SIO-IGPP.

554

555

556

## 557 **References**

- 558 Acuña, M.H., Connerney, J.E.P., Ness, N.F., Lin, R.P., Mitchell, D., Carlson, C.W., McFadden,  
559 J., Anderson, K.A., Rème, H., Mazelle, C., Vignes, D., Wasilewski, P., Cloutier, P., 1999.  
560 Global distribution of crustal magnetism discovered by the Mars Global Surveyor  
561 MAG/ER Experiment. *Science* 284, 790–793.
- 562 Alfé, D., Gillan, M. J., Price, G. D., 2002. Composition and temperature of the Earth's core  
563 constrained by combining ab initio calculations and seismic data. *Earth Planet. Sci.*  
564 *Lett.* 195, 91-98.
- 565 Allègre, C., Manhès, G., Lewin, E., 2001. Chemical composition of the Earth and the  
566 volatility control on planetary genetics. *Earth Planet. Sci. Lett.* 185, 49–69.
- 567 Anderson, O.L., Isaak, D. G., 2002. Another look at the core density deficit of Earth's  
568 outer core. *Phys. Earth Planet. Inter.* 131, 19-27.

569 Anderson, B.J., Johnson, C.L., Korth, H., Winslow, R.M., Borovsky, J.E., Purucker, M.E.,  
570 Slavin, J.A., Solomon, S.C., Zuber, M.t, McNutt Jr., R.L., 2012. Low-degree structure in  
571 Mercury's planetary magnetic field. *J. Geophys. Res.*, doi:10.1029/2012JE004159.

572 Andrault, D., Bolfan-Casanova, N., Ohtaka, O., Fukui, H., Arima, H., Fialin, M., Funakoshi,  
573 K., 2009. Melting diagrams of Fe-rich alloys determined from synchrotron in situ  
574 measurements in the 15–23GPa pressure range. *Phys. Earth Planet. Inter.* 174, 181-  
575 191.

576 Badro, J., Brodholt, J.P., Pieta, H., Siebert, J., Ryerson, F.J., 2015. Core formation and core  
577 composition from coupled geochemical and geophysical constraints. *PNAS*,  
578 [www.pnas.org/cgi/doi/10.1073/pnas.1505672112](http://www.pnas.org/cgi/doi/10.1073/pnas.1505672112).

579 Balog, P.S., Secco, R.A., Rubie, D.C., Frost, D.J., 2003. Equation of state of liquid Fe-10  
580 wt% S: implications for the metallic cores of planetary bodies. *J. Geophys. Res.*  
581 108(B2), 2124, doi: 10.1029/2001JB001646.

582 Birch, F., 1964. Density and composition of the mantle and core. *J. Geophys. Res.* 69,  
583 4377–4388.

584 Bland, M.T., Showma, A.P., Tobie, G., 2008. The production of Ganymede's magnetic  
585 field. *Icarus* 198, 384–399.

586 Braginsky, S., 1963. Structure of the F layer and reasons for convection in the Earth's  
587 core. *Sov. Phys. Dokl.* 149, 8-10.

588 Breuer, D., Rueckriemen, T., Spohn, T., 2015. Iron snow, crystal floats, and inner-core  
589 growth: modes of core solidification and implications for dynamos in terrestrial  
590 planets and moons. *Prog. Earth Planet. Sci.* 2:39, DOI 10.1186/s40645-015-0069-y.

591 Breuer, D., Spohn, T., 2006. Viscosity of the Martian mantle and its initial temperature:  
592 Constraints from crust formation history and the evolution of the magnetic field.  
593 Planet. Space Sci. 54, 153–169.

594 [Brodholt, J., and Badro, J., 2017. Composition of the low seismic velocity E0 layer at the  
595 top of Earth's core, Geophys. Res. Lett. 44, 8303–8310, doi:10.1002/2017GL074261.](#)

596

597 Buffett, B.A., Seagle, C.T., 2010. Stratification of the top of the core due to chemical  
598 interactions with the mantle. J. Geophys. Res. 115, B04407,  
599 doi:10.1029/2009JB006751.

600 [Buono, A.S., Walker, D., 2011. The Fe-rich liquidus in the Fe–FeS system from 1 bar to  
601 10 GPa. Geochim. Cosmochim. Acta 75, 2072-2087.](#)

602 Buono, A.S., Walker, D., 2015. H, not O or pressure, causes eutectic T depression in the  
603 Fe-FeS System to 8 GPa. Meteor. Planet. Sci. 50(4), 547–554.

604 Chabot, N.L., Drake, M.J., 1997. An experimental study of silver and palladium  
605 partitioning between solid and liquid metal, with applications to iron meteorites.  
606 Meteor. Planet. Sci. 32, 637-645.

607 Chen, B., Gao, L., Leinenweber, K., Wang, Y., Sanehira, T., Li, J., 2008a. In situ  
608 investigation of high-pressure melting behavior in the Fe-S system using synchrotron  
609 X-ray radiography. High Pressure Res. 28, 315-326, doi:  
610 10.1080/08957950802318883.

611 Chen, B., Li, J., Hauck II, S.A., 2008b. Non-ideal liquidus curve in the Fe-S system and  
612 Mercury's snowing core. Geophys. Res. Lett. 35, L07201,  
613 doi:10.1029/2008GL033311.

614 Christensen, U.R., 2015. Iron snow dynamo models for Ganymede. *Icarus* 247, 248–259.

615 Chudinovskikh, L., Boehler, R., 2007. Eutectic melting in the system Fe–S to 44 GPa.  
616 *Earth Planet. Sci. Lett.* 257, 97–103.

617 Davies, C. J., Pommier, A., 2015. Iron snow in the Martian core?, *Earth Planet. Sci. Lett.* In  
618 press.

619 Davies, C. J., Pozzo M., Gubbins, D., Alfè, D., 2015. Constraints from material properties  
620 on the dynamics and evolution of Earth’s core. *Nat. Geosci.* 8, 678–685,  
621 doi:10.1038/NNGEO2492.

622 Dreibus, G., Palme, H., 1996. Cosmochemical constraints on the sulfur content in the  
623 Earth’s core. *Geochem. Cosmochem. Acta* 60, 1125–1130.

624 Dreibus, G., Wänke, H., 1985. A volatile-rich planet. *Meteoritics* 20, 367–382.

625 Dumberry, M., Rivoldini, A., 2015. Mercury’s inner core size and core-crystallization  
626 regime. *Icarus* 248, 254–68.

627 Dwyer, C.A., Stevenson, D. J., Nimmo, F., 2011. A long-lived lunar dynamo driven by  
628 continuous mechanical stirring. *Nature* 479, 212–214.

629 Ehlers, E.G., 1972. *The Interpretation of Geological Phase Diagrams.* W.H. Freeman and  
630 Company.

631 Fei, Y., Bertka, C.M., 2005. The interior of Mars. *Science* 308, 1120–1121.

632 Fei, Y., Bertka, C.M., Prewitt, C.T., 2000. Structure type and bulk modulus of Fe<sub>3</sub>S, a new  
633 iron–sulfur compound. *Am. Miner.* 85, 1830–1833.

634 Fischer, R.A., Campbell, A.J., 2010. High-pressure melting of wüstite. *Am. Miner.* 95,  
635 1473–1477.

636 Frost, D. J., 2003. Fe<sup>2+</sup>-Mg partitioning between garnet, magnesiowustite, and (Mg,  
637 Fe)<sub>2</sub>SiO<sub>4</sub> phases of the transition zone. *Am. Miner.* 88, 387–397.

638 Gubbins, D., Alfè, D., Masters, G., Price, G.D., Gillan, M.J., 2003. Can the Earth's dynamo  
639 run on heat alone?. *Geophys. J. Int.* 155, 609–622.

640 Gubbins, D. Davies, C., 2013. The stratified layer at the core-mantle boundary caused by  
641 barodiffusion of oxygen, sulphur and silicon. *Phys. Earth Planet. Inter.* 215, 21-28.

642 Harder, H., Schubert, G., 2001. Sulfur in Mercury's Core?. *Icarus* 151, 118-122.

643 Hauck, II, S.A., Aurnou, J. M., Dombard, A. J., 2006. Sulfur's impact on core evolution and  
644 magnetic field generation on Ganymede. *J. Geophys. Res.* 111, E09008,  
645 doi:10.1029/2005JE002557.

646 Hauck, S.A., Phillips, R.J., 2002. Thermal and crustal evolution of Mars. *J. Geophys. Res.*,  
647 doi:10.1029/2001JE001801.

648 Hauck, S.A., Margot, J.L., Solomon, S.C., Phillips, R.J., Johnson, C.L., Lemoine, F.G.,  
649 Mazarico, E., McCoy, T.J., Padovan, S., Peale, S.J., Perry, M.E., Smith, D.E., Zuber, M.T.,  
650 2013. The curious case of Mercury's internal structure. *J. Geophys. Res.* 118, 1204–  
651 1220, doi:10.1002/jgre.20091.

652 Huang, H., Fei, Y., Cai, L., Jing, F., Hu, X., Xie, H., Zhang, L., Gong, Z., 2011. Evidence for an  
653 oxygen-depleted liquid outer core of the Earth. *Nature* 479, 513-516,  
654 doi:10.1038/nature10621.

655 Kamada, S., Ohtani, E., Fukui, H., Sakai, T., Terasaki, H., Takahashi, S., Shibazaki, Y.,  
656 Tsutsui, S.m Baron, A.Q.R., Hirao, N., and Ohishi, Y., 2014. The sound velocity  
657 measurements of Fe<sub>3</sub>S. *Am. Mineral.* 99, 98-101.

658 Kimura, J., Nakagawa, T., Kurita, K., 2009. Size and compositional constraints of  
659 Ganymede's metallic core for driving an active dynamo. *Icarus* 202, 216–24.

660 Kivelson, M. G., Khurana, K. K., Russell, C. T., Walker, R. J., Warnecke, J., Coroniti, F. V.,  
661 Polanskey, C., Southwood, D. J., Schubert, G., 1996. Discovery of Ganymede's magnetic  
662 field by the Galileo spacecraft. *Nature* 384, 537–541.

663 Komabayashi, T., 2014. Thermodynamics of melting relations in the system Fe-FeO at  
664 high pressure: Implications for oxygen in the Earth's core. *J. Geophys. Res.* doi:  
665 10.1002/2014JB010980.

666 Kondo, T., Ohtani, E., Hirao, N., Yagi, T., Kikegawa, T., 2004. Phase transitions of (Mg,  
667 Fe)O at megabar pressures. *Phys. Earth Planet. Inter.* 143–144, 201–213.

668 Laurenz, V., Rubie, D. C., Frost, D. J., Vogel, A. K., 2016. The importance of sulfur for the  
669 partitioning behaviour of the HSEs during Earth's differentiation. *Geochim.*  
670 *Cosmochim. Acta* 194, 123-138.

671 Le Bars, M., Wiczorek, M. A., Karatekin, Ö., Cébron, D., Laneuville, M., 2011. An impact-  
672 driven dynamo for the early Moon. *Nature* 479, 215-218.

673 Li, J., Fei, Y., Mao, H.K., Hirose, K., Shieh, S.R., 2001. Sulfur in the Earth's inner core. *Earth*  
674 *Planet. Sci. Lett.* 193, 509-514.

675 Lister, J.R., Buffett, B.A., 1995. The strength and efficiency of thermal and compositional  
676 convection in the geodynamo. *Phys. Earth Planet. Int.* 91, 17-30.

677 Malavergne, V., Toplis, M.J., Berthet, S., Jones, J., 2010. Highly reducing conditions during  
678 core formation on Mercury: implications for internal structure and the origin of a  
679 magnetic field. *Icarus* 206, 199–209.

680 Mann, U., Frost, D.J., Rubie, D.C., 2009. Evidence for high-pressure core-mantle  
681 differentiation from the metal-silicate partitioning of lithophile and weakly-  
682 siderophile elements. *Geochim. Cosmochim. Acta.* 73, 7360–7386.

683 Martorell, B., Brodholt, J., Wood, I. G., Vocadlo, L., 2013. The effect of nickel on the  
684 properties of iron at the conditions of Earth's inner core: Ab initio calculations of  
685 seismic wave velocities of Fe–Ni alloys. *Earth Planet. Sci. Lett.* 365, 143-151.

686 McDonough, W.F., Sun, S.-S., 1995. The composition of the Earth. *Chem. Geol.* 120, 223–  
687 253.

688 [Mori, Y., Ozawa, H., Hirose, K., Sinmyo, R., Tateno, S., Morard, G., Ohishi, Y., 2017. Melting  
689 experiments on Fe–Fe<sub>3</sub>S system to 254 GPa. \*Earth Planet. Sci. Lett.\* 464, 135-141.](#)

690 Murakami, M., Hirose, K., Ono, S., Tsuchiya, T., Isshiki, M., Watanuki, T., 2004. High  
691 pressure and high temperature phase transitions of FeO. *Phys. Earth Planet. Inter.*  
692 146, 273–282.

693 Ness, N.F., Behannon, K.W., Lepping, R.P., Whang, Y.C., 1975. Magnetic field of Mercury. *J.*  
694 *Geophys. Res.* 80, 2708–2716.

695 Nimmo, F., 2015. Thermal and compositional evolution of the core. in *Treatise on*  
696 *Geophysics*, 2nd edn, Vol. 9 (ed. Schubert, G.), 201-219.

697 Nishida, K., Terasaki, H., Ohtani, E., Suzuki, A., 2008. The effect of sulfur content on  
698 density of the liquid Fe–S at high pressure. *Phys. Chem. Minerals* 35, 417–423.

699 Ohtani, E., Ringwood, A.E., 1984. Composition of the core, I. Solubility of oxygen in  
700 molten iron at high temperatures. *Earth Planet. Sci. Lett.* 71, 85-93.

701 O'Neill, H. St. C, 1991. The origin of the Moon and the early history of the Earth- A  
702 chemical model. Part 2: The Earth. *Geochim. Cosmochim. Acta* 55, 1159-1172.



703 Poirier, J.-P., Light elements in the Earth's outer core: A critical .1994 review. *Phys. Earth*  
704 *Planet. Int.* 85, 319-337.

705 Righter, K., Sutton, K.R., Danielson, L., Pando, K., Newville, M., 2016. Redox variations in  
706 the inner Solar System with new constraints from vanadium XANES in spinels. *Am.*  
707 *Mineral.* 101, 9-10, 1928-1942.

708 Ringwood, A.E., Hibberson, W., 1991. Solubilities of mantle oxides in molten iron at high  
709 pressures and temperatures" implications for the composition and formation of  
710 Earth's core. *Earth Planet. Sci. Lett.* 102, 235-251.

711 Rubie, D.C., 1999. Characterising the sample environment in multianvil high-pressure  
712 experiments. *Phase Transitions* 68, 431-451.

713 Rubie, D.C., Gessman, C.K., Frost, D.J., 2004. Partitioning of oxygen during core formation  
714 on the Earth and Mars. *Nature* 429, 58-61.

715 Rubie, D.C., Laurenz, V., Jacobson, S.A., Morbidelli, A., Palme, H., Vogel, A.K., Frost, D.J.,  
716 2016. Highly siderophile elements were stripped from Earth's mantle by iron sulfide  
717 segregation. *Science* 353, 1141-1144.

718 Rückriemen, T., Breuer, D., Spohn, T., 2015. The Fe-snow regime in Ganymede's core: a  
719 deep seated dynamo below a stable snow zone. *J. Geophys. Res.* 120, 1095-1118.

720 Sanloup, C., Fei, Y., 2004. Closure of the Fe-S-Si liquid miscibility gap at high pressure.  
721 *Phys. Earth Planet. Int.* 147, 57-65.

722 Sanloup, C., Guyot, F., Gillet, P., Fiquet, G., Mezouar, M., Martinez, I., 2000. Density  
723 measurements of liquid Fe-S alloys at high-pressure. *Geophys. Res. Lett.* 27, 811-814.

724 Sanloup, C., Jambon, A., Gillet, P., 1999. A simple chondritic model of Mars. *Phys. Earth*  
725 *Planet. Inter.* 112, 43-54.

726 Schubert, G., Anderson, J. D., Spohn, T., McKinnon, W. B., 2004. Interior composition,  
727 structure and dynamics of the Galilean satellites, in *Jupiter: The Planet, Satellites, and*  
728 *Magnetosphere*, edited by F. Bagenal, T. Dowling, and W. B. McKinnon, pp. 281–306,  
729 Cambridge Univ. Press, New York.

730 Shibazaki, Y., Ohtani, E., Terasaki, H., Tateyama, R., Sakamaki, T., Tsuchiya, T., Funakoshi,  
731 K., 2011. Effect of hydrogen on the melting temperature of FeS at high pressure:  
732 Implications for the core of Ganymede. *Earth Planet. Sci. Lett.* 301, 153–158.

733 Solomon, S.C., Aharonson, O., Aurnou, J.M., Banerdt, W.B., Carr, M.H., Dombard, A.J., Frey,  
734 H.V., Golombek, M.P., Hauck II, S.A., Head III, J.W., Jakosky, B.M., Johnson, C.L.,  
735 McGovern, P.J., Neumann, G.A., Phillips, R.J., Smith, D.E., Zuber, M.T., 2005. New  
736 perspectives on ancient Mars. *Science* 307, 1214–1220.

737 Stevenson, D.J., Spohn, T., Schubert, G., 1983. Magnetism and thermal evolution of the  
738 terrestrial planets. *Icarus* 54, 466–89.

739 Stewart, A. J., Schmidt, M. W., van Westrenen, W., Liebske, C., 2007. Mars: A new core-  
740 crystallization regime. *Science* 316, 1323–1325.

741 Tsuno, K., Ohtani, E., 2009. Eutectic temperatures and melting relations in the Fe–O–S  
742 system at high pressures and temperatures. *Phys. Chem. Miner.* 36, 9–17.

743 Tsuno, K., Ohtani, E., Terasaki, H., 2007. Immiscible two-liquid regions in the Fe–O–S  
744 system at high pressure: Implications for planetary cores. *Phys. Earth Planet. Int.*  
745 160, 75–85.

746 Tsuno, K., Frost, D.J., Rubie, D.C., 2011. The effects of nickel and sulphur on the core–  
747 mantle partitioning of oxygen in Earth and Mars. *Phys. Earth Planet. Int.* 185, 1–12.

748 Urakawa, S., Kato, M., Kumazawa, M., 1987. Experimental study on the phase relations  
749 in the system Fe–Ni–O–S. High-pressure research in mineral physics. Tokyo:  
750 TERRAPUB, 95–111.

751 Urakawa, S., Someya, K., Terasaki, H., Katsura, T., Yokoshi, S., Funakoshi, K., Utsumi, W.,  
752 Katayama, Y., Sueda, U., Irifune, T., 2004. Phase relationships and equations of state  
753 for FeS at high pressures and temperatures and implications for the internal  
754 structure of Mars. *Phys. Earth Planet. Int.* 143/144, 469–479.

755 Vilim, R., Stanley, S., Hauck, S.A., 2010. Iron snow zones as a mechanism for generating  
756 Mercury's weak observed magnetic field. *J. Geophys. Res.* 115, E11003,  
757 doi:10.1029/2009JE003528.

758 Walker, D., 2000. Core participation in mantle geochemistry: Geochemical Society  
759 Ingerson Lecture, GSA Denver, October 1999. *Geochim. Cosmochim. Acta* 64 (17),  
760 2897–2911.

761 Wicht, J., Heyner, D., 2014. Mercury's magnetic field in the messenger era. In: Shuanggen  
762 J., editor, *Planetary geodesy and remote sensing*. London: CRC Press.

763 Williams, J.-P., Nimmo, F., 2004. Thermal evolution of the Martian core: Implications for  
764 an early dynamo. *Geology* 32 (2), 97-100.

765 Wood, B.J., Walter, W.J., Wade, J., 2006. Accretion of the Earth and segregation of its  
766 core. *Nature* 441, 825–833.

767

768

769

770

771 **Figure captions**

772

773 Figure 1: Back-scattered electron images of run products in the Fe-S system. A) Fe,  
774 5wt.% S, 20 GPa, 1760°C (S6413): fully molten sample showing Fe dendrites in an FeS  
775 matrix (dark grey); B) Fe, 5wt.% S, 20 GPa, 1400°C (S6418): large pure iron grains  
776 (right) coexist with quenched FeS liquid (left); C) Fe, 1wt.% S, 20 GPa, 1850°C (S6431):  
777 the iron matrix (bottom) containing a few FeO grains (black) is overlain by FeS liquid;  
778 D) Zoom in from C) in the quenched liquid area showing iron dendrites in an FeS  
779 matrix. Area of solid accumulation are expected to be slightly cooler than the top part of  
780 the capsule, suggesting that melt separates from the solid phase due to a small  
781 temperature gradient rather than density contrast (see text for details).

782

783 Figure 2: Phase relations in the Fe-S and Fe-S-O systems at 14 and 20 GPa (based on  
784 microprobe analyses on retrieved experimental samples). Each dot indicates the S and  
785 O contents in the liquid and is located at the corresponding S content of the liquid phase  
786 (except for experiments containing 35wt%S as the liquid phase was not analyzed). The  
787 data from two experiments are not plotted (S6433a and S6520a) as bulk melt analyses  
788 (defocused beam) were not performed. Grey lines are from previous studies at similar  
789 pressure (Fei et al., 2000; Chen et al., 2008a). The phases observed in the Fe-S-O system  
790 are labeled in green. Numbers in italic are wt. S in the liquid phase coexisting with metal  
791 Fe (Fe-S system). The red dashed line indicates a possible corrected FeS liquidus (see  
792 text for details). No significant effect of oxygen on liquidus temperature is observed.

793

794 Figure 3: Back-scattered electron images of run products in the Fe-S-O system. A)  
795 Sample containing 0.65wt.% O quenched at 1760°C and 20 GPa (S6426). Fe dendrites  
796 (light grey) coexist with FeS matrix and FeO (dark grey) is present in the quenched  
797 liquid as rosaceous grains; B) Sample containing 3wt.% O quenched at 1400°C and 20  
798 GPa (S6428). FeO is present as isolated grains (dark grey) in solid iron. The absence of  
799 an FeO layer at the liquid/solid interface suggests that the layer stability is temperature  
800 dependent (see text for details); C) Sample containing 3wt.% O and quenched at 1400°C  
801 and 14 GPa showing the presence of a continuous FeO layer at the liquid/solid interface  
802 (S6433b); D) FeO layer (gray) in sample containing 3 wt.% O, 14 GPa, 1500°C (H4277);  
803 E) and F): destruction of the FeO layer at 14 GPa, 1400°C (S6535a, E)) and 20 GPa,  
804 1600°C (S6520a, F)). [Area of solid accumulation are expected to be slightly cooler than  
805 the top part of the capsule, suggesting that melt separates from the solid phase due to a  
806 small temperature gradient rather than density contrast \(see text for details\).](#)

807

808 Figure 4: Sulfur and oxygen solubilities in solid iron and liquid. A) Amounts of S in the  
809 iron metal phase as a function of temperature and comparison with previous studies. O  
810 contents in the solid phase were about 0.2 at.% or less. B) Concentration of S in the  
811 liquid phase for samples with (filled circles) and without (open circles) oxygen added as  
812 a function of temperature at 14 and 20 GPa. A general trend suggests a decrease in S  
813 content with increasing the degree of partial melting. C) Concentration of O in the liquid  
814 phase as a function of temperature at 14 and 20 GPa. The amount of oxygen in the liquid  
815 phase increases up to ~1wt.% with increasing temperature.

816

817 Figure 5: Oxygen fugacity expressed relative to the Iron-Wüstite buffer as a function of  
818 temperature. Redox conditions were calculated for each sample using the formalism of  
819 Mann et al., 2009 based on the FeO content in the MgO capsule (Fe-S system) or  
820 considering  $X_{\text{FeO}}=1$  (FeO buffered experiments in the Fe-S-O system). Estimates of  
821 oxygen fugacity for present-day Martian lower mantle are shown for comparison and  
822 come from Righter et al., 2016 and references therein. See text for details.

823

824 Figure 6: Evolutionary scenarios of the cooling core of a terrestrial planet, considering a  
825 Fe-S-O composition with potentially the addition of other elements (such as Si). Top  
826 panel: top-down crystallization (snow regime), bottom panel: bottom-up crystallization  
827 (inner core). Both scenarios present stages of gravitational instability and all contribute  
828 to decrease the dynamo activity. In a snowing core, the presence of FeO decreases the  
829 magnetic activity by reducing the thermal gradient and may cause to the cessation of  
830 the dynamo. In an inner core crystallization regime, the presence of FeO at the solid  
831 inner core-liquid interface initially helps the dynamo by enhancing convection. The  
832 subsequent upward migration of FeO due to density contrast with coexisting phases  
833 then weakens the magnetic field. The heat production related to the formation of solid  
834 FeO is labeled  $Q_{\text{FeO}}$ . See text for details.

835

836 Figure 7: Pressure-temperature diagram showing experiments from this study and  
837 previous works in the Fe-S-O system (green data points), and comparison with the  
838 present-day thermal structure of Mars (maroon), Mercury (purple), and Ganymede  
839 (orange). Shaded areas are defined by possible adiabats for each planet from previous

840 modeling studies (Breuer et al., 2015 for Ganymede; Harder and Schubert, 2001 for  
841 Mercury; Williams and Nimmo, 2004, Fei and Bertka, 2005, Hauck and Phillips, 2002 for  
842 Mars). Fe-S (5wt.%S) melting curve from Chen et al., 2008b; iron melting curve and Fe-S  
843 eutectic from Chen et al., 2008b redrawn from Boehler, 1993; Fei et al., 1997. The  
844 presence of solid FeO at the solid Fe - liquid interface (green lines) is derived from our  
845 experiments and previous studies that observed FeO at the same interface (Buono and  
846 Walker, 2015) or not (Urakawa et al., 1987; Tsuno and Ohtani, 2009). The thermal  
847 structure of the three bodies considered overlaps the stability field of FeO and may have  
848 been compatible with the formation of solid FeO at the solid-liquid interface at some  
849 stage of core cooling, depending on the crystallization regime.

850

851

852

853